



Article

Modeling Land Use Transformations and Flood Hazard on Ibaraki's Coastal in 2030: A Scenario-Based Approach Amid Population Fluctuations

Mohammadreza Safabakhshpachekhenari * and Hideyuki Tonooka

Graduate School of Science and Engineering, Ibaraki University, Hitachi 316-8511, Ibaraki, Japan; hideyuki.tonooka.dr@vc.ibaraki.ac.jp

* Correspondence: 20nd305g@vc.ibaraki.ac.jp

Abstract: Coastal areas, influenced by human activity and natural factors, face major environmental shifts, including climate-induced flood risks. This highlights the importance of forecasting coastal land use for effective flood defense and ecological conservation. Japan's distinct demographic path necessitates flexible strategies for managing its urban development. The study examines the Ibaraki Coastal region to analyze the impacts of land-use changes in 2030, predicting and evaluating future floods from intensified high tides and waves in scenario-based forecasts. The future roughness map is derived from projected land-use changes, and we utilize this information in DioVISTA 3.5.0 software to simulate flood scenarios. Finally, we analyzed the overlap between simulated floods and each land-use category. The results indicate since 2020, built-up areas have increased by 52.37 sq. km (39%). In scenarios of constant or shrinking urban areas, grassland increased by 28.54 sq. km (42%), and urban land cover decreased by 7.47 sq. km (5.6%) over ten years. Our research examines two separate peaks in water levels associated with urban flooding. Using 2030 land use maps and a peak height of 4 m, which is the lower limit of the maximum run-up height due to storm surge expected in the study area, 4.71 sq. km of residential areas flooded in the urban growth scenario, compared to 4.01 sq. km in the stagnant scenario and 3.96 sq. km in the shrinkage scenario. With the upper limit of 7.2 m, which is the extreme case in most of the study area, these areas increased to 49.91 sq. km, 42.52 sq. km, and 42.31 sq. km, respectively. The simulation highlights future flood-prone urban areas for each scenario, guiding targeted flood prevention efforts.

Keywords: remote sensing; flood; storm surge simulations; future land use; Japan's population contraction; neural network; maximum entropy classifier



Citation: Safabakhshpachekhenari, M.; Tonooka, H. Modeling Land Use Transformations and Flood Hazard on Ibaraki's Coastal in 2030: A Scenario-Based Approach Amid Population Fluctuations. *Remote Sens.* **2024**, *16*, 898. <https://doi.org/10.3390/rs16050898>

Academic Editors: Yuji Murayama, Ahmed Derdouri and Ruci Wang

Received: 13 January 2024

Revised: 26 February 2024

Accepted: 1 March 2024

Published: 3 March 2024



Copyright: © 2024 by the authors. Licensee MDPI, Basel, Switzerland. This article is an open access article distributed under the terms and conditions of the Creative Commons Attribution (CC BY) license (<https://creativecommons.org/licenses/by/4.0/>).

1. Introduction

Climate change in the 21st century intertwines a spectrum of risks, including severe weather, rising sea levels, altered precipitation, biodiversity loss, and increased environmental contamination [1]. Around 25% of people worldwide live in coastal urban areas, predominantly in major rivers' deltas and estuaries [2]. Significant and widespread effects of coastal flooding are evident globally, especially in these delta cities [3]. About 85% of these deltas have recently experienced extensive flooding, leading to nearly 260,000 km² of terrain inundation [4]. Studies show that despite attempts to decrease greenhouse gas emissions, the continuous rise in worldwide sea levels and an increase in severe storm events will inevitably lead to greater flood risks in the years ahead [5,6].

Japan, characterized by its long history of coping with earthquakes, storm surges, and tsunamis, can be described as a disaster-prone society. The unique topography of Japan, where steep, mountainous regions comprise 61% of the landscape, largely dictates the patterns of human settlement and infrastructure development [7]. The challenging landscape drives about 49% of the population to settle in the more accessible low-lying coastal areas, where 75% of the nation's real estate is concentrated [8]. In March 2011,

Japan faced a record 9.0 magnitude earthquake, triggering a massive tsunami with waves reaching 15 m [9]. This disaster, striking the Tohoku region, resulted in 16,000 deaths and 2000 missing and caused \$122 billion in damages [9,10]. It also led to a nuclear crisis at the Fukushima Daiichi Nuclear Power Plant, bringing environmental and power challenges. Recent natural disasters have underscored the delicate balance urban settlements in seaside regions precariously maintain with their natural surroundings [11,12].

The restricted comprehension of flood impacts often leads to inadequate government funding for climate adaptation efforts, whereas present adaptation actions often overlook the spatial dimensions and consequences of flooding [13,14]. Addressing flood-related analytical studies in urban land-use development is as vital as implementing mitigation strategies to safeguard urban infrastructure, residents, and edifices [15]. Fusing climate change knowledge with advanced coastal management techniques is imperative to revolutionize coastal planning [15]. This synergy will spark the creation of innovative spatial tools, transforming land-use strategies and elevating our capacity to adjust to and mitigate climate impacts in coastal regions.

Several research initiatives have employed remote sensing and spatial modeling techniques alongside GIS-based analyses of tsunamis, rising sea levels, and frequent storm surges to meet this requirement. For instance, Canters et al. [16] integrate a GIS-based flood hazard model with a cellular automata land-use change model, creating risk maps for the Belgian coast. The study, focusing on 1000-year and 4000-year storms, highlights significant changes in land use and population risk, emphasizing the importance of considering land-use dynamics in coastal flood hazard assessments. Barry et al. [17] adopted a combined decision-making approach and analytical hierarchy process, incorporating sea level rise into urban land suitability evaluations, suggesting improvements in future land development by considering environmental adaptability. Miller et al. [18] comprehensively analyzed projected flood hazards in Southeastern Texas, synthesizing scenarios like land subsidence, rising sea levels, and storm surges to quantify the extent of flooding. Their study suggests that merging remote sensing methods with simulation models can yield precise measurements of land elevation changes and detailed flood models, offering valuable insights for future urban and regional planning. The central theme among the other studies emphasizes utilizing computational scenario-based assessment in planning and designing flood risk mitigation strategies, a practical and holistic approach to addressing the complexities and pinpointing the most vulnerable locations [19,20]. The reported methods lacked consideration for future land classified map-based roughness and a more accurate comparison of future land use/land cover (LULC) models in scenario-based flood risk assessments.

In reviewing the literature focused on studies within the Japan-centric area in this field, it is noteworthy to mention several valuable research works, including Moya et al. [21], explored the use of machine learning and remote sensing with historical disaster data for quick post-disaster damage detection and testing on the 2018 Okayama rainfall and 2019 Typhoon Hagibis in Japan. Results showed a moderate correlation with official flood maps, suggesting the effectiveness of past data in real-time disaster analysis. Also, Liu et al. [22] presented a simple method for emergency response using Sentinel-1 SAR images to analyze flood impacts from Typhoon Hagibis in Ibaraki. Focusing on the Naka and Kuji rivers, it combines change detection and a novel index for complete and partial flood mapping, validated against official data, achieving 74% accuracy. Ohki et al. [23] developed a method for flood detection by combining ALOS-2 satellite data and hydrodynamic simulations, using Bayesian inference for integrating various data types. Tested on 12 Japanese floods, it proved accurate and computationally efficient, showing promise for daily monitoring. However, in these reported studies, essential aspects were not accounted for, such as the spatiotemporal LULC under targeted scenarios linked to population dynamics and even future risks stemming from the highest levels of tsunamis or storm surges.

Despite global population growth, some developed countries like Japan expect significant demographic decreases [24], and this demands a reassessment of their land-use

change [25]. Population decline impacts urban area intricately [26,27]. Therefore, evaluating Japan's urban trajectories is vital [28], with scenarios ranging from urban stabilization and potentially shrinking to growth via rejuvenation measures and population growth incentives by the government. Hence, future strategies must account for these dynamic elements, reimagining what urban changes mean in the face of Japan's unique demographic trajectory. Therefore, as a disaster society, developments should consider new techniques to enhance urban oceanfront resilience; the process relies on predictive modeling for scenario-driven urban-environmental changes, integrating demographic effects and leveraging computational scenario-based assessment to identify areas most at risk of flooding.

This study elaborates on a methodology integrating future LULC simulation models for 2030 based on three scenarios for flood risk assessment, considering variations in two distinct tidal levels. This model collaboratively combines an artificial neural network-based multilayer perceptron (ANN-MLP) and a Markov chain (MC) model to upgrade projections of nonlinear land-use transformation while taking into account parameters related to the topographical characteristics, accessibility considerations, and demographic factors, extracting the patterns inferred from historical transitions by the maximum entropy classifier, serving as a supplementary input to enhance the generalizability of the model. The ultimate objective is to estimate flooding and inundation impacts in the coastal area of Ibaraki, Japan, and evaluate their adaptation effectiveness by exemplifying the amalgamation of the simulation model with storm surge inundation. The results of this study contribute to the creation of efficient spatial planning approaches for climate-resilient coastal cities, accommodation, and situations with decreasing populations.

2. Materials and Methods

2.1. Study Area

Ibaraki Prefecture, located in Japan's Kantō region, is home to over 2.8 million people and covers 6097 km². It borders Fukushima, Tochigi, Saitama, Chiba Prefectures, and the Pacific Ocean. In Ibaraki Prefecture, amid a trend of depopulation and rising vacant homes, new house construction is paradoxically on the rise [29]. This is happening alongside substantial infrastructure developments driven by government rejuvenation policies [30]. Key initiatives include the Townscape Renewal for Urban Beautification, Naka River Improvement for a safer, more prosperous city, disaster-resilient road construction, community revival through tunnel projects, the development of Hitachinaka port, enhanced living and urban growth via the Tsukuba Express, and tourism enhancement through new attractions [30]. These diverse efforts illustrate the complex trajectory of Ibaraki's future transformation. The study area, which is the southern Ibaraki Coast, is illustrated in Figure 1.

It is a region of ecological richness where the warm Kuroshio and cold Oyashio currents meet, fostering diverse marine life. This coastline is an ecological treasure and a strategic industrial hub, hosting key ports like Ibaraki and Kashima, which are crucial for logistics in eastern Japan. However, balancing coastal conservation with sustainable use is essential, especially after the 2011 Great East Japan Earthquake [31]. This disaster underscored the need for disaster-resilient coasts and effective tsunami countermeasures. The vision for the Ibaraki coast is to create a safe, prosperous area that benefits everyone, achieved through collaborative efforts between the community and government. Unfortunately, the coast faces challenges like erosion, storm surges, and the ever-present tsunami threat [32]. In response, the Japanese government has developed new tsunami strategies based on lessons from past disasters, aiming to define and protect crucial areas along the Ibaraki coast to ensure safety [32]. These measures include fortifications against common, lower height Level 1 tsunamis and extensive evacuation plans for the less frequent but more devastating Level 2 tsunamis. Additionally, strategies are in place to mitigate the effects of storm surges and the anticipated 50-year probability wave [32].

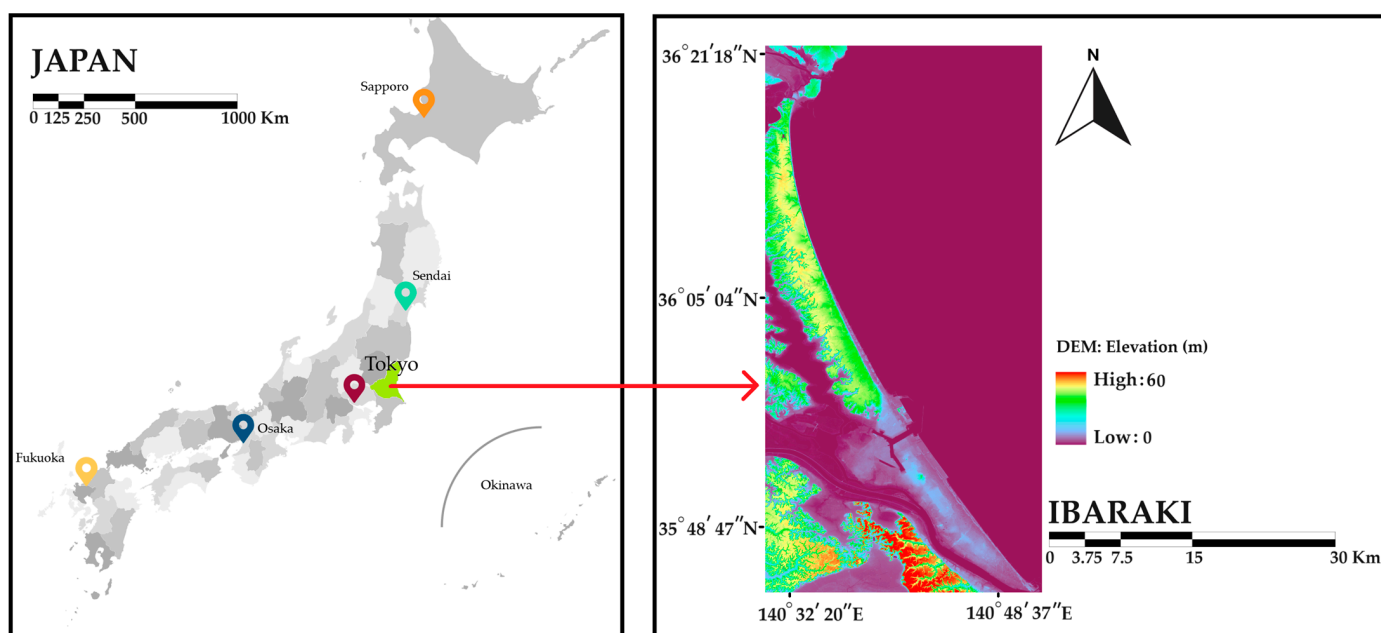


Figure 1. Location of the study area.

2.2. Datasets

In our study, we analyzed the impact of land changes using detailed LULC maps. These maps, covering the periods 2006–2011 and 2018–2020, were generated by the Earth Observation Research Center at the Japan Aerospace Exploration Agency (JAXA) [33]. JAXA employed advanced Earth observation techniques, utilizing satellite data for comprehensive regional and national analysis. The data for these maps were sourced using JAXA from a variety of comprehensive datasets. This included high-resolution images from Sentinel-2 Level-1C accessed through the Google Earth Engine API, data from ALOS-2/PALSAR-2, and extensive data points from the SACLAJ database incorporating ground surveys and digital interpretations. The ALOS PRISM Digital Surface Model, a slope analysis derived from this model and a vegetation map for bamboo forests by the Biodiversity Center were also used. Data on solar cell panel locations were from Electrical Japan and coastal line data were from the Geospatial Information Authority of Japan.

In addition to the LULC maps, we incorporated the Digital Elevation Model (DEM) into our data collection. This DEM, offering a detailed spatial resolution of 5 m, was obtained from the Geospatial Information Authority of Japan [34]. Additionally, we used spatial population distribution data from WorldPop, associated with the School of Geography and Environmental Science at the University of Southampton [35]. Our study also included future population estimation data organized in 500 m mesh grids provided by the Ministry of Land, Infrastructure, Transport, and Tourism [36]. We also utilized OpenStreetMap's road network data to generate raster maps illustrating distances from roads. Similarly, this same data source was employed for creating the road map itself.

2.3. Methodology

2.3.1. Overview

This study introduces a methodology for predicting future urban land changes and assessing flood risks based on scenario-based projections. Initially, the LULC maps from JAXA (spanning 2006–2011 and 2018–2020) are reclassified into ten distinct categories. These include water bodies, built-up areas, paddy fields, and a variety of forest types such as deciduous broad-leaf forest (DBF), deciduous needle-leaf forest (DNF), evergreen broad-leaf forest (EBF), and evergreen needle-leaf forest (ENF). The next step involves preparing explanatory variables, which, together with LULC maps, serve as the input for the ANN-MLP. These encompass a range of factors such as DEM, slope, proximity to urban

areas, roads, and best-fit polynomial-based trend surfaces. Given that city shrinkage is closely tied to demographic factors, special emphasis is placed on these considerations. We sourced a set of demographic data from the Japanese census and developed some indicators to illustrate the study area's population characteristics, such as the spatial distribution of the population, the distribution of people over 65 years old, and the population change rate maps. These data, along with other variables, are also incorporated as input into the ANN-MLP.

Furthermore, the maximum entropy classifier is employed to generate another input variable, thereby enhancing the analysis. This statistical model was leveraged to discover each pixel's likelihood of change or stasis before it occurs and to provide a clear view of both changes and continuities in land use. These insights are then integrated into the ANN-MLP, alongside other explanatory variables, to refine the understanding and prediction of land use dynamics.

Machine learning algorithms like ANN-MLP analyze land use demand and distribution by understanding the causal links between historical land-use changes and their driving factors.

The ANN-MLP model was employed under three distinct urban scenarios: firstly, considering urban expansion; secondly, under a scenario of static urban growth with increased emphasis on other land categories; and thirdly, in the context of urban contraction. Following establishing transition potentials for land-use change, we employed a Markov chain model to forecast land-use demands for the years 2023 and 2030. Subsequently, we evaluated the accuracy of our projected 2023 land-use map. Upon validation, we generated roughness map values using the 2030 LULC maps. The second phase of our study also involved the creation of embankment data, which is crucial for precise flood modeling.

Integrating roughness map values and embankment data into the DioVISTA 3.5.0 flood simulator software [37] enabled the simulation of future storm surge inundation, considering two scenarios involving high tide and waves. These simulations were grounded on the temporal change in the water level specified by a storm surge associated with typhoon.

Utilizing ArcGIS for spatial analysis, we determined the extent of flooding in urban regions across all three projected LULC scenarios for 2030, considering various flood conditions. Consequently, our study presents a method for developing detailed and flexible approaches, like managing flood risks in oceanfront towns, using our scenario-oriented flood risk evaluation framework. Figure 2 provides a comprehensive visual depiction of the entire methodological process.

2.3.2. Collection and Creation of Explanatory Variables

Within the framework of spatiotemporal simulation, the task of defining modeling variables is critical, as it directly affects the spatial distribution patterns of LULC [38]. Hence, the chosen factors must incorporate a balanced consideration of demographic–morphologic–accessibility elements to ensure a comprehensive and precise simulation of land-use change [39].

In contemporary urban studies, the concept of urban shrinkage—essentially the counterpoint to urbanization—is gaining prominence [40]. This phenomenon, characterized predominantly by a declining population, has become a salient feature in the scholarly discourse on shrinking cities [41,42]. Japan stands out as a notable example in this context, given its distinction as one of the few nations experiencing a negative population growth trajectory [43]. In examining the interplay of factors influencing urban shrinkage, it is evident that in Japan, there is a synchronous occurrence of urban shrinkage and urban sprawl when viewed from a spatial pattern perspective [40]. Therefore, it is imperative that future land use planning, in the context of depopulation, incorporates scenarios that address both infrastructure development and urban shrinkage dynamics. This approach should also consider the implications for urban areas should they achieve stability without further shrinkage.

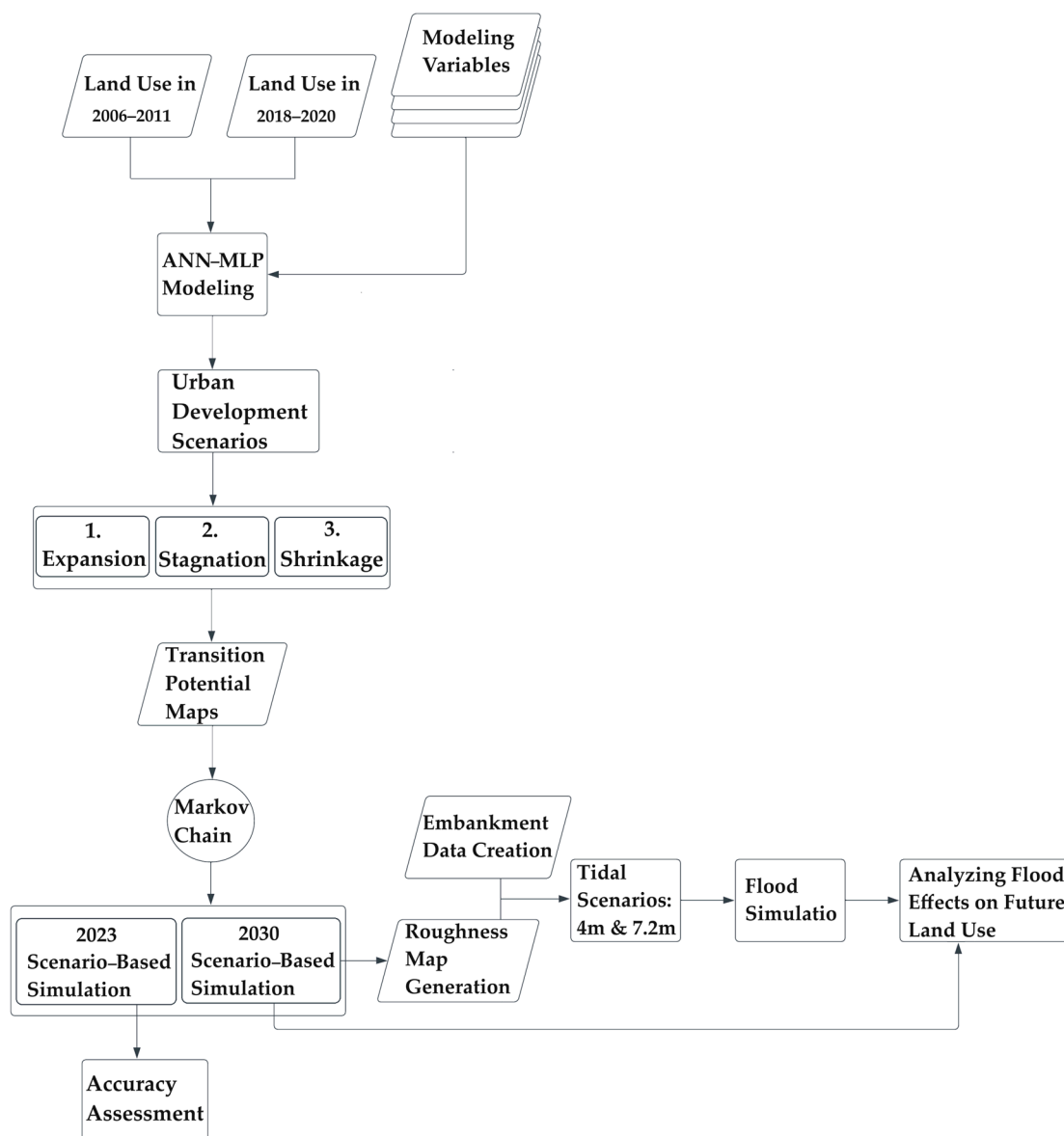


Figure 2. A comprehensive scenario-based framework for future flood risk assessment.

Since a significant correlation exists between the demographic aged 65 and older and the prevalence of vacant housing units [44], so a spatial distribution map of the population over 65 was generated as driver variables from 500 m mesh future population estimates provided by Japan’s National Land Information Division, MLIT. Also, this research developed the Population Change Rate (PCR) [45] between two distinct study years to quantify the extent of shrinkage, proximity to populated areas, and spatial distribution of population, considering these aspects as additional explanatory factors. The selection of other change agents encompassed a DEM, slope, road map, proximity to roads and urban areas, and the spatial trend of change. The preparation of all these data was conducted using ArcGIS Pro version 10.8.2. At last, we utilized the MASK tool to standardize the spatial extent and pixel size of all datasets according to the classified map of the study area.

In addition, with the aim of including temporal transition probability distribution analysis, our approach involved utilizing a map delineating primary transitions and areas of persistence (no change) as dependent variables. These were analyzed in conjunction with independent variables, such as proximity to population centers in 2011, 2015, and 2020, along with DEM, slope, and road network data. This analysis was conducted using a maximum entropy classification method [46,47], within the TerrSet 2020 IDRISI software.

As a result, we generated maps illustrating the probabilities of transitions before their occurrence through statistical insight. Characterizing these interactions improves the ANN-MLP learning process [48]. All explanatory variables are shown in Figure 3.

2.3.3. Artificial Neural Network-Based Multi-Layer Perceptron and Markov Chain Model

A computational model known as an artificial neural network is designed to emulate the workings of the human brain's biological systems. Renowned as a highly effective method for processing extensive data sets, this approach excels at performing computational tasks that involve identifying patterns, discerning trends, and providing predictive insights [49]. Among several types of ANN, the MLP is distinguished as a feed-forward network. Its key characteristics include ease of implementation, the ability to develop superior models, and relatively shorter training times compared to complex alternatives [50].

The algorithm's structure is organized into three primary segments: the input section (comprising variables or driving factors), the concealed intermediary layers, and the final output layers. These segments are each made up of numerous neurons. The concealed layers are recipients of values originating from the initial input layers. Subsequently, a designated weight is computed and conveyed along with the total values to the output layers, where the outcomes are derived. The procedure is as follows [50]:

$$\text{LULC}_i = f\left(\sum_{j=1}^n W_{i,j} X_j + b_i\right) \quad (1)$$

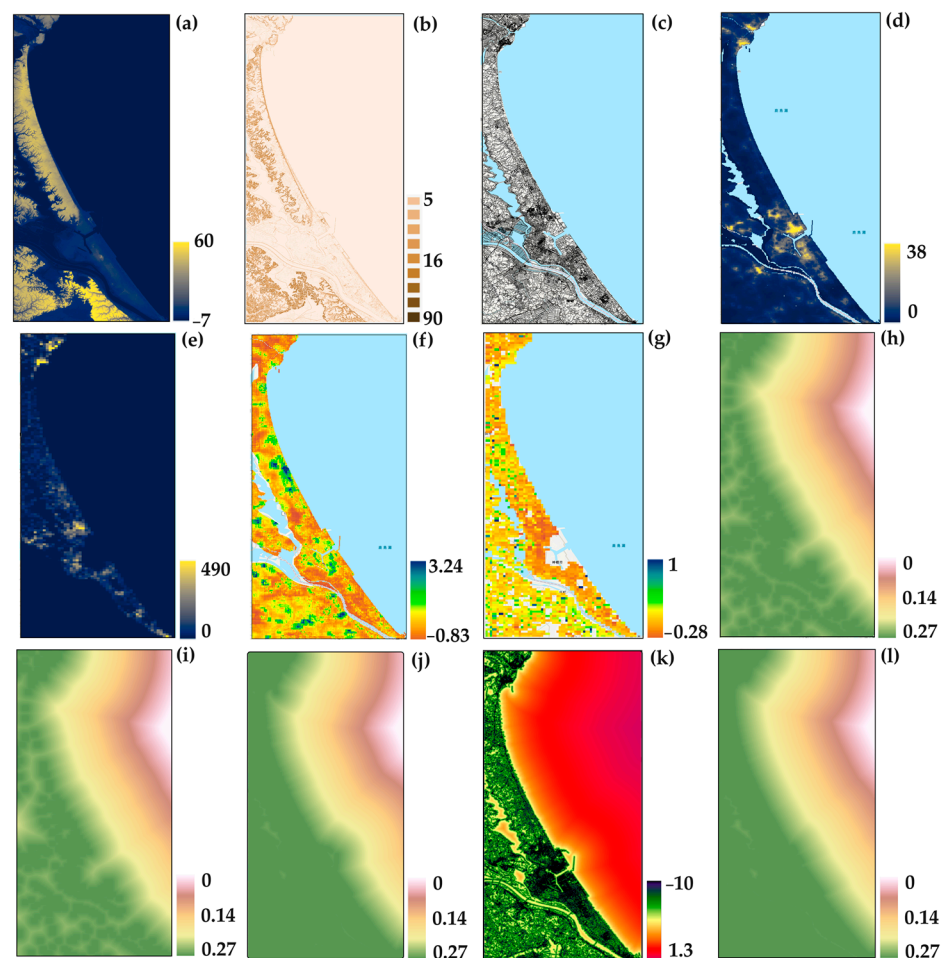


Figure 3. Cont.

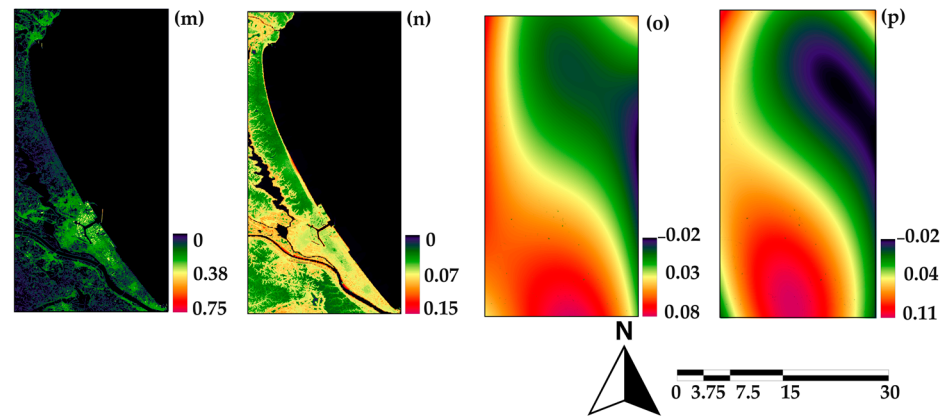


Figure 3. Spatial patterns of change agents: (a) DEM, (b) slope, (c) road map, (d) distribution of the population (100 m), (e) distribution of ages 65 and older (500 m), (f) population change rate from 2011 to 2020 (100 m), (g) population change rate from 2020 to 2030 (100 m), (h) distance to the population in 2025 (500 m), (i) distance to the population in 2030 (500 m), (j) distance to road and railways, (k) natural log transformation, (l) distance to urban area in 2023, (m) probability distribution of historical transitions (to urban areas), (n) probability distribution of historical transitions (to non-urban areas), (o) spatial trend of change (to non-urban areas), (p) spatial trend of change (to urban areas).

In this model, $LULC_i$ represents the output at node i , where f is the activation function. x denotes inputs (x_1, x_2, \dots, x_n), and w stands for weights ($w_{1j}, \dots, w_{ij}, \dots, w_{nj}$), with w_{ij} being the weight from node i to j . b_i is a bias term that helps optimize the model. In an MLP, the value of a neuron N is calculated based on these parameters.

$$Q_n = \sum_{j=1}^k W_{k,j} X_j \quad (2)$$

In the configuration of neuron n , Q_n is formulated as a linear amalgamation. The elements $w_{k1}, w_{k2}, \dots, w_{kn}$, signify the neurotransmission weights of neuron n . The computation of neuron n 's output hinges on this combination:

$$y_n = \varphi(u_N - \theta_N) \quad (3)$$

where φ is the action function and θ_k is the threshold. In neural networks, activation functions are crucial as they help map inputs to outputs, enabling the network to represent and process complex data patterns. This function, often the sigmoid type in hidden or output layers, can vary across nodes or be uniformly applied. In other words, the training involves a back-propagation algorithm in MLP, which conducts nonlinear statistical regression.

Integrating the Markov chain with MLP forms a hybrid model, enhancing the precision of MLP forecasts [49]. MCs operate on the principle of stochastic processes, where transition probabilities between discrete states are empirically determined [51]. This model begins in one of the various states and transitions sequentially through them, each representing a step. Each state is influenced solely by its immediate predecessor in a first-order MC, whereas higher-order MCs consider multiple preceding states [52].

Applying the Markov chain model in this study focuses on predicting dynamic land-use changes with high accuracy and operational precision. A transfer matrix is developed by analyzing land-use data from two different years to understand the transformation relationships between various land-use types. The formula is as follows [53]:

$$P = \begin{bmatrix} p_{11} & \dots & p_{1n} & \dots & p_{n1} & \dots & p_{nn} \end{bmatrix} \quad (4)$$

where n represents the total number of land-use types, the matrix P is the transition probability matrix, where each element p_{ij} indicates the probability of land-use type i

changing to type j . The indices i and j label the initial and subsequent land-use types, respectively. Each probability element p_{ij} must be between 0 and 1, as they represent the likelihood of one land-use type converting to another.

Thus, in the MLP-MC model, a two-step process is employed for test data prediction. Initially, the MLP is utilized to generate an initial prediction. Subsequently, the model computes the discrepancies between these predictions and the actual values, referred to as residual errors [53]. To enhance prediction accuracy, the MLP-MC model incorporates the analysis of residual error transitions via Markov transition matrices. It leverages this analysis to make appropriate adjustments, ultimately yielding refined predictions based on the insights derived from these matrices.

2.3.4. Design for Future High Tide and Wave Crest Scenarios on the Ibaraki Coastline

Addressing the likelihood of coastal flooding in the future involves understanding several intricate elements, including storm surges and rising sea levels. Storm surges are typically linked with weather systems characterized by low pressure, including tropical and intense extratropical cyclones. Meanwhile, the future trajectory of the sea level is closely tied to the patterns of future emissions, which remain a significant area of uncertainty.

The enactment of the “Revised Coastal Law” of Japan in April 2000 introduced two new goals: “environmental improvement and conservation” and “sustainable coastal utilization”, complementing the existing focus on “protection (disaster prevention)”. Following this amendment, Ibaraki Prefecture developed the Ibaraki Coastal Protection Master Plan [32]. This plan was crafted in alignment with the government’s “Basic Policy for Coastal Protection”, integrating feedback from local communities and considering both the environmental attributes and the utilization of the coastline. Figure 4 presents the procedures for establishing the targeted height of embankment in accordance with the Ibaraki Coastal Protection Master Plan.

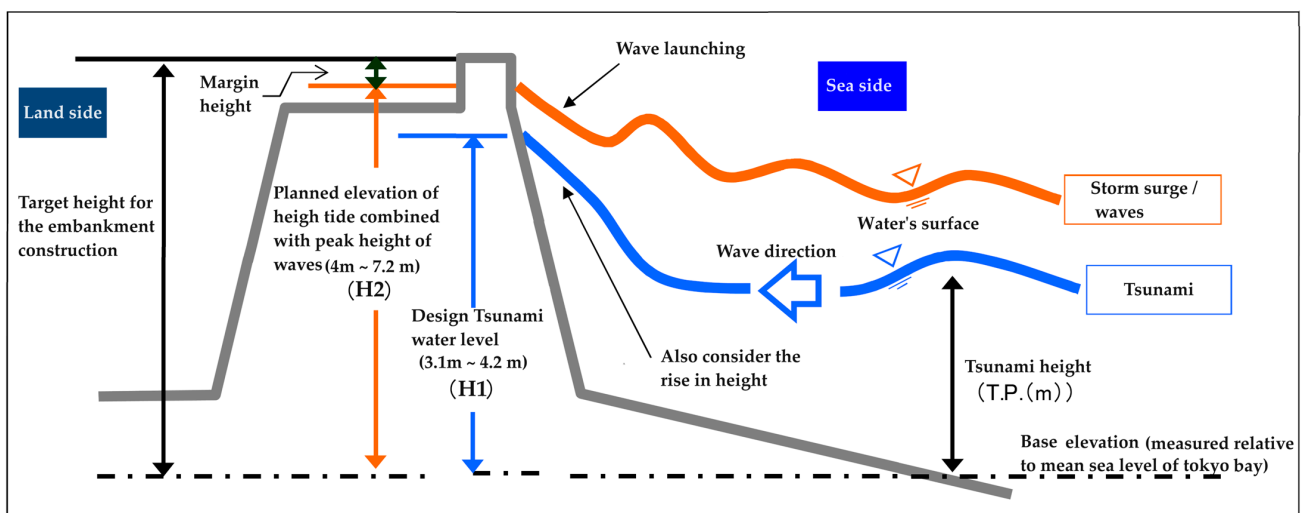


Figure 4. Procedures for establishing the aimed height of embankment according to the Ibaraki Coastal Protection Master Plan. This figure was produced from Figure 3.1 in [32].

The target embankment height is calculated by selecting the higher value between the “design tsunami level (H1)” and the “(H2) that denotes the surge/waves-induced run-up height” and then incorporating an additional safety margin. This height is recognized as the utmost level along the regional coastline.

When a typhoon’s winds blow seawater toward the coast, it causes a rise in sea level known as the “drift effect” [54]. This rise is proportional to the square of the wind speed; doubling the wind speed quadruples the sea level rise [54]. In V-shaped bays, the narrowing topography further amplifies this rise. Additionally, a typhoon’s decreasing atmospheric pressure also elevates sea levels. This combined effect results in a storm

surge, with the difference from the normal astronomical tide level termed as the tidal level deviation (actual tide level = astronomical tide level + tidal level deviation). The H1 and H2 designations represent anticipated water levels that may occur infrequently, ranging from several decades to a few centuries [32]. Specifically, these levels predict a rise in water height varying from 4 m in Tokai Village Shirakata and Hitachinaka Ichizaki Town, to 7.2 m in Hirai Kashima City and Hikawa Kamisu City [32]. Such estimates are vital for the planning and construction of embankments, serving as critical measures to safeguard human lives, residential properties, and the local economy against these rare but significant water level increases.

Numerical models utilizing two-dimensional shallow water equations are frequently employed for precise flood simulation [55]. The effectiveness of these models has been confirmed through various validations [56]. The relevant equations are described below [55]:

$$i = \frac{\delta h}{\delta t} + \frac{\delta(uh)}{\delta x} + \frac{\delta(vh)}{\delta y} \quad (5)$$

$$\frac{\delta(uh)}{\delta t} = -gh \frac{\delta H}{\delta x} - \frac{gr^2}{h^{\frac{4}{3}}} (uh) \sqrt{u^2 + v^2} \quad (6)$$

$$\frac{\delta(vh)}{\delta t} = -gh \frac{\delta H}{\delta y} - \frac{gr^2}{h^{\frac{4}{3}}} (vh) \sqrt{u^2 + v^2} \quad (7)$$

In this context, ' h ' represents the depth of the water, while ' H ' denotes the overall water level ($h + L$, (where ' L ' is the elevation of the ground)). The terms ' u ' and ' v ' are used to describe the velocity components along the x-axis and y-axis, respectively. The symbol ' g ' stands for the acceleration due to gravity and the letter ' t ' represents time. The variable ' r ' refers to the coefficient of Manning's roughness and ' i ' indicates the quantity of vertical inflow.

We utilized DioVISTA, a flood simulation software that effectively integrates with geographic information systems for commercial facility flood-risk assessments [57]. It offers a user-friendly interface and quick and accurate flood scenario simulations and was crucial in assessing risks for an entertainment complex near two rivers [57]. The software efficiently predicts severe flooding impacts, aiding in evacuation strategies [58]. Its capabilities include automatic area calculation, topographic data acquisition, and rapid results output. The Dynamic DDM was used to implement the numerical model with the function that automatically defines the calculation area and rapidly outputs the results [58].

2.3.5. Verification of Projected LULC Maps for Different Scenarios

Our evaluation encompassed three predictive maps, leveraging a robust array of metrics specifically curated for land-use change simulation science. This set of metrics, comprising both categorical and binary accuracy assessments, allowed for an in-depth analysis of each model's performance. For categorical evaluations, we used kappa coefficients, while binary accuracy within urban pixels was assessed using the F1 score, Matthew's correlation coefficient (MCC), receiver operating characteristic (ROC), and Youden's J. This comprehensive approach facilitated a detailed evaluation of the effectiveness of each predictive model.

To give a clearer perspective, Cohen's kappa coefficient evaluates the agreement between two variables, typically for interrater reliability. It ranges from -1 to 1 , where 1 signifies total agreement, and 0 indicates none. Negative values imply agreement below the chance level. While a not universally accepted "good" kappa exists, values above 0.75 are often considered excellent, following Fleiss' guidelines [59].

Binary metrics are also crucial in urban pixel analysis. The F1 score, a balanced measurement of precision and recall, is particularly effective in uneven class distributions. It evaluates both the relevance of selected instances and the selection of relevant examples [59]. MCC offers a comprehensive assessment for binary classifications by considering all confusion matrix values, ensuring balance even in imbalanced distributions [60]. Together,

these metrics thoroughly understand model performance in various land-use categories, balancing precision-recall and accurate classification rates. Additionally, the ROC curve and its area under the curve (AUC) are robust tools for evaluating the model's ability to differentiate between urban and non-urban categories. Additionally, Youden's J Index is valuable for pinpointing the optimal threshold for classifying a pixel as urban or non-urban. Maximizing the sum of sensitivity and specificity helps achieve the best possible accuracy in urban pixel predictions, considering both the presence and absence of urban characteristics. Figure 5 presents the diagram of statistical evaluations, offering a clear understanding.

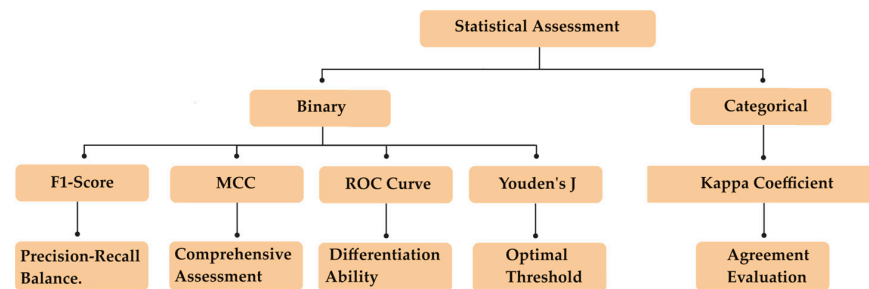


Figure 5. Statistical assessments and their applications.

3. Results

3.1. Comparative Analysis of Land Use: Initial Map (2006–2011) versus Second Map (2018–2020)

The analysis results of the two maps, as shown in Figure 6, reflect anthropogenic and demographic influences on terrestrial landscapes between two temporal datasets. The pronounced increase in built-up areas indicates urbanization, likely driven by rejuvenation measures, infrastructure development, and population growth incentives. Conversely, the decline in paddy fields and cropland may be linked to the overall contraction in the number of farming households. Notably, only the segment of large-scale farmers, those managing 3.0 hectares or larger, is on the rise. In contrast, there is a noticeable decrease in the number of farmers who operate farms ranging from 0.3 to 3.0 hectares. Expanding grassland areas may suggest reversing cropland and paddy lands due to abandonment. The transformation of barren landscapes into grasslands in Japan can likely be linked to its warm, moist climate, fostering a spontaneous ecological shift in unattended areas. In particular, around 16 km² of paddy fields were transformed into grasslands, and concurrently, approximately 10 km² of cropland underwent a similar transition to grassland. Moreover, there was a marked trend of cropland and barren land being predominantly repurposed for urban development. Also, EBF and DBF, which are vital types of vegetation within terrestrial ecosystems crucial for maintaining sustainable biodiversity and integral in the global carbon cycling process, have also undergone a transition, resulting in their conversion into grasslands.

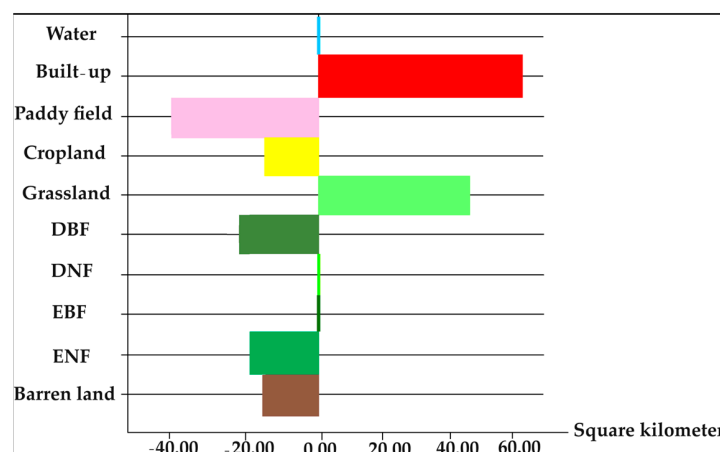


Figure 6. Net change in different categories of land classification between 2006–2011 to 2018–2020.

We conducted a detailed follow-up on the land use map's pixels, indicating a reduction in urban areas. Cross-referencing these changes with Google Earth Pro confirmed the decline in specific urban locations. Figure 7 illustrates two instances of the cases discussed.



Figure 7. Two instances of urban decline.

Consequently, drawing on substantial evidence, this study examines the specified region through three separate scenarios. The first scenario predicts expansion in urban areas. The second scenario envisions a steady urban landscape, coupled with an increase in grasslands as the manifest of abandoned agricultural lands. The third scenario projects a tendency towards a decrease in urban expanses.

3.2. Contribution of Each Explanatory Variables in ANN-MLP

The ANN-MLP model was employed to generate predictions for three distinct future land use scenarios in the specified area. In each iteration, the model's inputs, or driving forces, were uniquely tailored to align with the specific characteristics of the respective scenario. The idea was to encapsulate traditional data sources with more dynamic and temporal streams that could signal transitions in land use. In Table 1, we illustrate the model's sensitivity when independent variables are held constant. The table provides a quantified look at how each independent variable affects the model's accuracy, and we can extract valuable information. Firstly, the model's performance metrics, such as accuracy rate and skill measure, offer valuable insights into the ANN model's overall effectiveness under varied conditions with each variable maintained constant. Secondly, the influence of variables, which involves ranking the independent variables based on their impact on the model's output, provides an understanding of the influence order of these inputs on the model. This ranking helps understand which variables are most and least important in determining the model's outcome. This is a common approach to understanding the robustness of the model concerning its inputs.

In the case of urban growth, maintaining a constant natural logarithm of distance to urban areas in the model hinders its ability to distinguish proximity to urban centers, thus leading to a less nuanced understanding of urban expansion patterns. Thus, it is deemed the most crucial variable. Additionally, by holding DEM constant, the model cannot account for the constraints or opportunities that topography presents for urban expansion. Ignoring the historical likelihood of a transition to urban land use also affects the model's predictive accuracy by omitting the temporal aspect of how spatial factors influence urban expansion. The spatial distribution of the population aged 65+ and the transition probability of pixels that changed to grassland (before their conversions) perform a pivotal role in the generalizability of ANN-MLP in the case of expanding grasslands. This observation highlights the apparent reality that individuals within this age group generally exhibit lower demand for urban expansion and are less active in the workforce. Consequently, this correlates with the increase in grasslands due to the decline in agricultural activities and the stagnation of urban regions. Additionally, the initial transition probability of pixels still serves as a meaningful pattern for predicting future developments. Hence,

keeping them constant removes essential variance and the information that the model needs to predict transitions accurately. In the third scenario, the shrinking urban areas are influenced not only by the aging population and the region's topography but also by the rate of population change.

Table 1. Forcing a single independent variable to be constant.

Simulation Scenario	Explanatory Variables	Accuracy Rate	Skill Measure	Influence Order
1- Urban Expansion	1- Proximity to the urban center	60.95	0.5313	4
	2- Proximity to dense population	60.80	0.5296	7
	3- DEM	46.61	0.3593	2
	4- Probability distribution of transition to urban	50.49	0.4059	3
	5- Urban spatial trends	55.68	0.4682	10
	6- Nlog transformation of urban distance	34.87	0.2184	1
	7- PCR (2020–2025)	57.59	0.4911	5
	8- Slope	60.92	0.5310	8
	9- Proximity to the road	60.93	0.5312	9
	10- Road map	60.72	0.5286	6
2- Urban Stability and Grassland Expansion	1- Proximity to dense population	45.75	0.2767	4
	2- Population distribution	45.55	0.2740	3
	3- Population distribution age 65+	43.48	0.2464	2
	4- Probability distribution of transition to grassland	35.14	0.1352	1
	5- PCR (2011–2020)	45.81	0.2775	7
	6- PCR (2020–2030)	46.31	0.2841	11
	7- Proximity to dense population of 2025	45.82	0.2776	10
	8- DEM	45.80	0.2773	6
	9- Slope	45.81	0.2775	8
	10- Proximity to the urban center	45.82	0.2775	9
	11- Grassland spatial trends	45.78	0.2571	5
3- Urban Shrinkage	1- Proximity to dense population	53.94	0.3091	6
	2- Population distribution	54.77	0.3215	9
	3- Population distribution age 65+	44.57	0.1686	1
	4- Probability distribution of shrinkage	51.03	0.2654	4
	5- PCR (2011–2020)	53.85	0.3077	5
	6- PCR (2020–2030)	49.54	0.2431	3
	7- Proximity to dense population of 2025	54.01	0.3102	7
	8- DEM	46.54	0.1980	2
	9- Slope	54.78	0.3218	10
	10- Proximity to dense population of 2030	54.88	0.3231	11
	11- Shrinking spatial trends	54.34	0.3152	8

Other variables with intermediate influence also contribute to the model's predictions to varying degrees and may also be necessary depending on the specific context or application of the model.

3.3. Model Validation and Accuracy

The study involved a detailed analysis of three LULC projection maps for 2023, employing a variety of metrics to assess the model's efficacy in predicting changes in land classes. The change in pixel numbers, relative to the overall size of the area under study, was relatively minor. This observation led to the adoption of the kappa coefficient for a broad categorical evaluation alongside binary metrics explicitly aimed at determining the accuracy of urban pixel predictions, a key focus of this research. Comprehensive results, including the F1 score, MCC, ROC curve, AUC, and Youden's J index, are thoroughly presented in Table 2 and Figure 8. These findings demonstrate that while the three scenarios achieved high scores in the kappa coefficient, there were significant differences in their F1

and MCC scores. This variation highlights the critical role of binary metrics in urban land use mapping as a necessary supplement to categorical evaluations.

Table 2. LULC prediction assessment with kappa, F1, and MCC metrics.

Indicators	Simulation Scenario		
	1- Urban Expansion	2- Urban Stability and Grassland Expansion	3- Urban Shrinkage
Kappa	88.66	85.33	88.22
F1 score	0.8568	0.7912	0.7817
MCC	0.7001	0.5461	0.5255

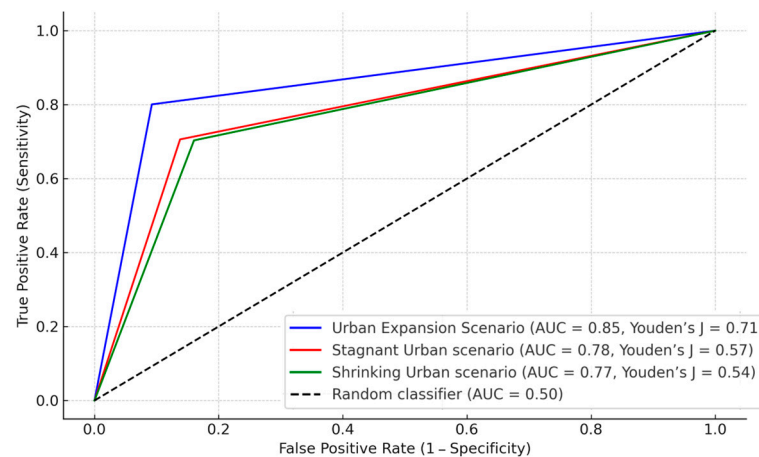


Figure 8. Assessing model performance through ROC curves, AUC metrics, and Youden's index analysis.

With a closer look, it is evident that the kappa coefficients for Scenarios 1 and 3 differ by only 0.44, yet both outperform Scenario 2, which has a kappa value of 0.8533. Scenario 2's kappa score is approximately 3% lower than the others. This discrepancy may be attributed to overestimating the increased rate of abandoned agricultural lands and grasslands. In reality, the transformation of cropland and paddy fields into grasslands is occurring at a slower pace and to a lesser extent than predicted, leading to a marginally lower kappa score for Scenario 2.

In the first scenario, notable distinctions set it apart from the other two, reflected in its superior performance across all binary evaluation metrics. This scenario achieved an F1 score of 0.8568 and a MCC of 0.7001. The MCC, known for its rigor, considers all aspects of the confusion matrix (true positives, false negatives, true negatives, and false positives). This comprehensive approach means the MCC often yields lower values compared to the F1 score, particularly when false positives or negatives are high. Despite a large number of true positives that might inflate the F1 score, the MCC remains more balanced, penalizing classification errors more evenly.

Scenarios 2 and 3 exhibit closely matched performance metrics. Despite their differing methodologies, these simulations show a comparable accuracy in predicting outcomes, possibly due to some overlap in the urban categories they analyze. However, a slight variance is noticeable, with Scenario 2 marginally outperforming Scenario 3 by 0.0206 in MCC and 0.03 in Youden's J index. A plausible explanation could be the urban shrink has a slow trend, which is very likely.

3.4. Modeling Future LULC Scenarios 2030 and Generating Roughness Maps Based on Predicted Outcomes

Following the validation of our 2023 data, we projected LULC maps for the year 2030. Our findings indicate a significant expansion of urban areas, increasing by 52.37 km² (39%)

since 2020. Additionally, under a hypothetical scenario where urban expansion remains constant, we observed an increase of 28.54 km² (42%) in grassland areas. In a contrasting scenario where urban areas contract, we noted a decrease of 7.47 km² (5.6%) in urban land cover over these ten years.

In simulating storm surge inundation, while ideally the simulation would incorporate detailed representations of buildings and other structures in the topography, practical limitations like computational demands and data preparation costs necessitate a simpler approach. Thus, land use is typically represented by roughness coefficients. For coastal floods, the Manning roughness coefficient is varied based on land use, reflecting the varying degrees of resistance encountered in different environments, such as urban areas with dense building coverage. A standard value of approximately 0.025 (m^{-1/3}s) is used for sea regions. We create roughness maps based on the coefficients in the storm surge inundation simulation guide [61] released by the Coastal Office, Water Management and Land Conservation Bureau, Ministry of Land, Infrastructure, Transport, and Tourism. According to this guideline, the roughness coefficients for different land types are as follows: urban areas have a coefficient of 0.04, paddy fields and croplands are assigned a value of 0.02, grassland is at 0.025, while DBF, DNF, EBF, and ENF all have a coefficient of 0.03. Barren lands and water bodies are also assigned a roughness coefficient of 0.025.

To create a roughness map, we utilize the raster calculator tool within ArcGIS Pro. The outcomes of the Land Use and Land Cover (LULC) maps for the year 2030, along with the roughness maps, are presented in Figures 9 and 10, respectively.

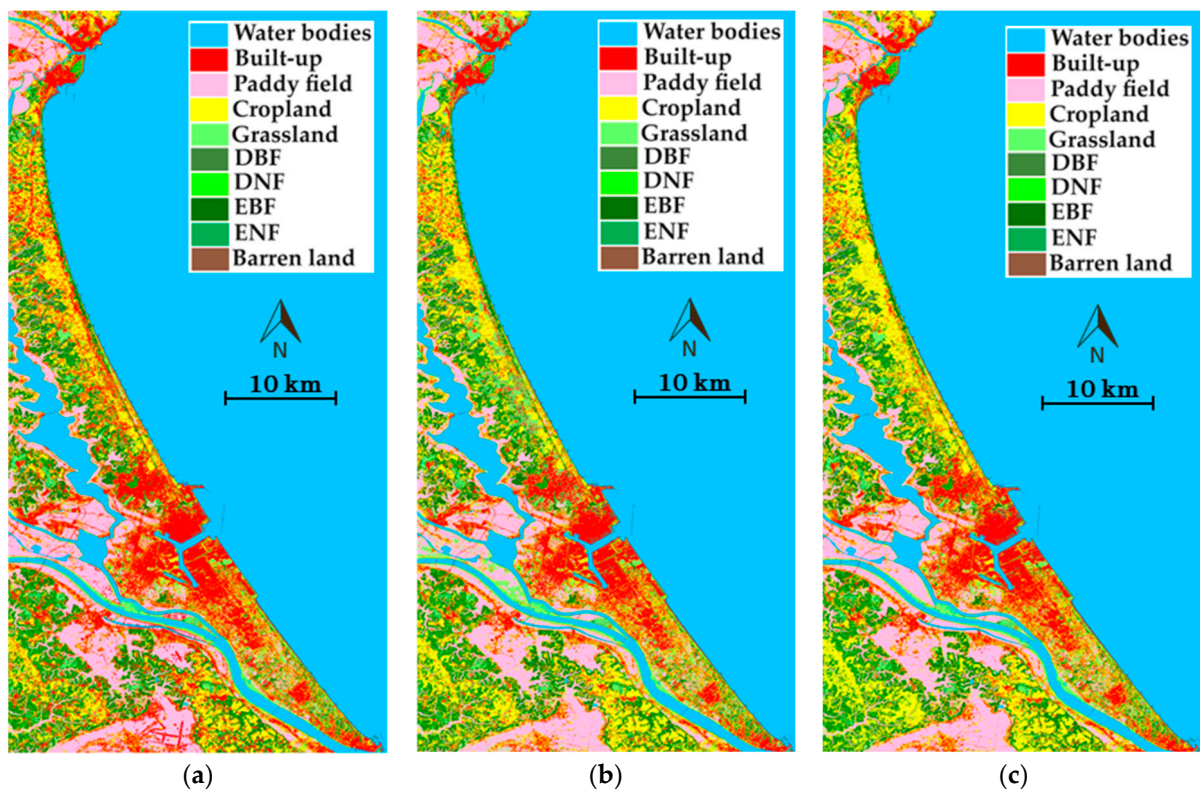


Figure 9. Spatial distribution of predicted LULC dynamics: (a) projected LULC in 2030 based on Scenario 1, (b) projected LULC in 2030 based on Scenario 2, and (c) projected LULC in 2030 based on Scenario 3.

3.5. Flood Scenario Simulation with Input Water Levels

In the preceding stage, we developed a roughness coefficient map, which was then transformed into text data for integration with the DioVISTA flood simulator software. Concurrently, we generated a shapefile for the embankment, extracting precise coordinates from Google Earth Pro for the designated study area. This facilitated the creation of an

accurate embankment model in the DioVISTA software, incorporating real-world data pertaining to its height. For effective flood modeling within DioVISTA, we constructed a 10 m mesh grid, incorporating the embankment, roughness data and DEM. This setup enabled us to conduct simulations for the year 2030. We conducted simulations of flood scenarios based on two distinct peak conditions: a typhoon coinciding with the highest tide. These scenarios generated a peak height of 4 m, which is the lower limit of the maximum run-up height due to storm surge expected in the study area and the upper limit of 7.2 m, indicative of extreme cases in most parts of the study area. The time variation in the input water level for these simulations, which replicated the pattern of the storm surge mechanism caused by typhoon (the occasion that happened in Osaka on 4 September 2018), is illustrated in Figure 11. The outcomes of these simulations are also presented in Figure 12.

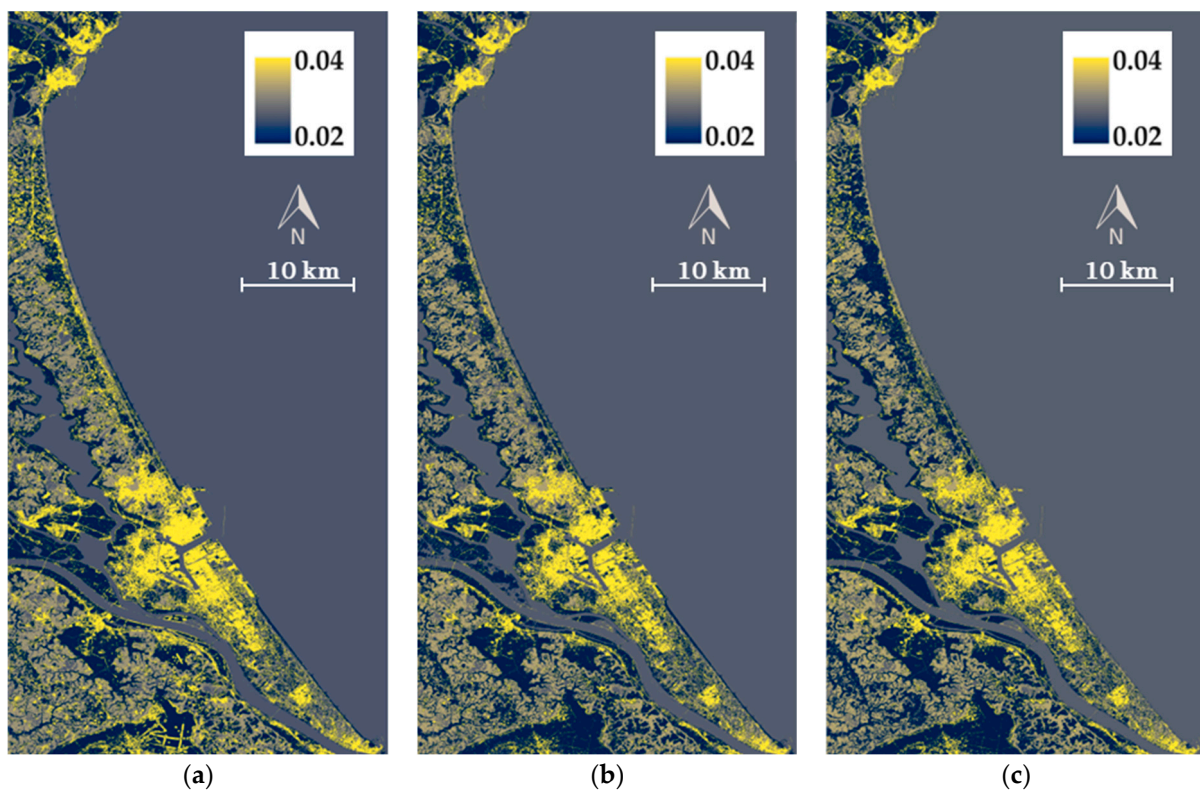


Figure 10. Projected LULC-based roughness coefficient map: (a) roughness coefficient map based on Scenario 1, (b) roughness coefficient map based on Scenario 2, and (c) roughness coefficient map based on Scenario 3.

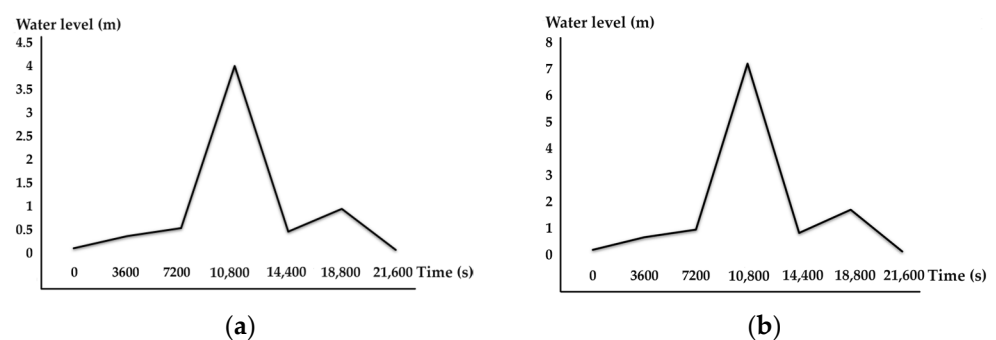


Figure 11. The time variation in the input water levels: (a) water level reaches its peak at 4 m, (b) water level reaches its peak at 7.2 m.

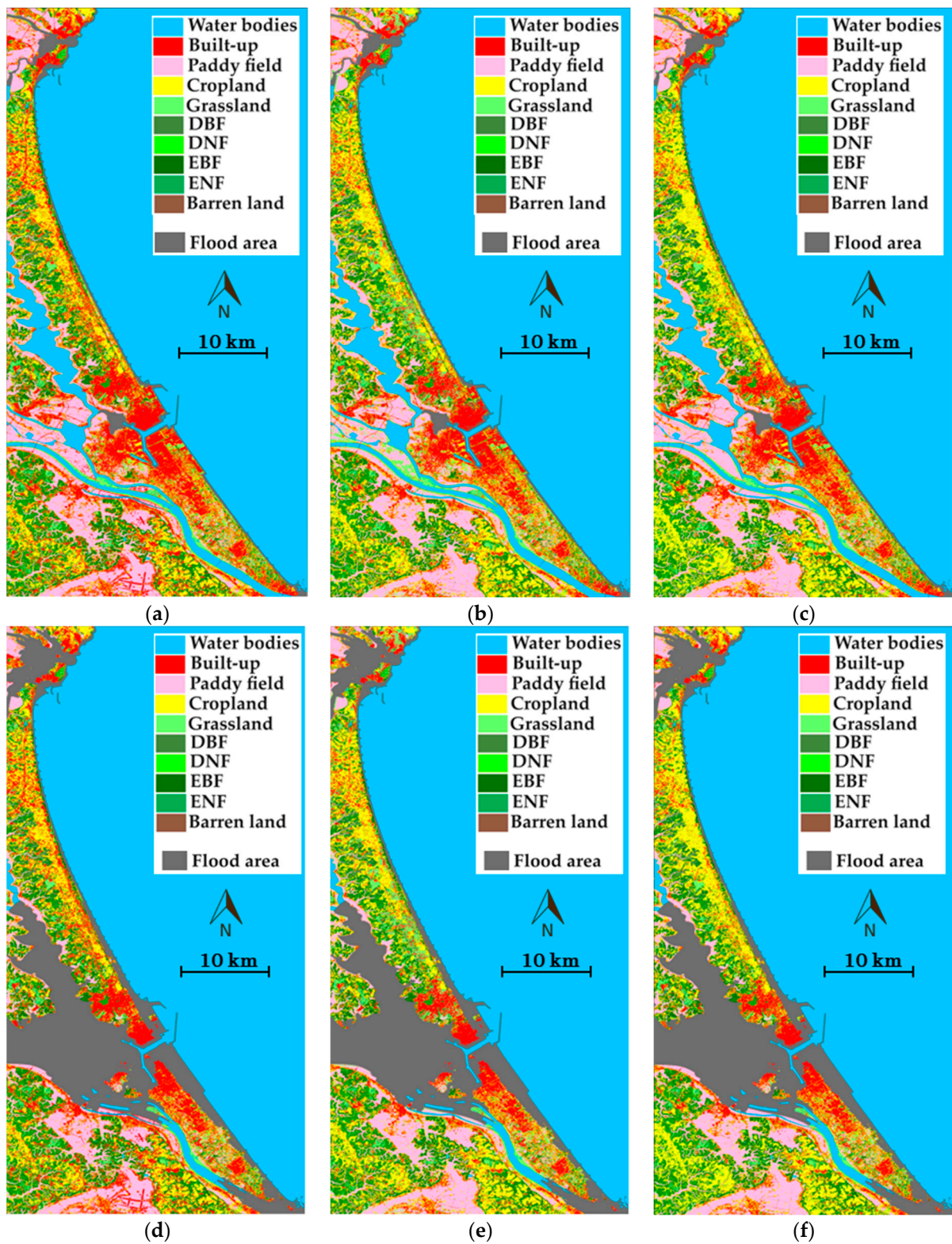


Figure 12. Simulation outcomes for flood patterns under diverse LULC scenarios in 2030. (a–c) are the results with a peak height of 4 m, which is the lower limit of the maximum run-up height due to storm surge expected in the study area: (a) the urban expansion scenario, (b) urban stability, grassland spread scenario, and (c) urban shrinkage scenario. (d–f) are the results with the upper limit of 7.2 m, which is the extreme case in most of the study area: (d) urban expansion scenario, (e) urban stability, grassland spread scenario, and (f) urban shrinkage scenario.

We began by rasterizing flood data and aligning coordinates, then separated urban pixels from 2030 LULC maps for a detailed analysis of urban flood impact. Our findings revealed that at a water level increase of 4 m, the extent of flooding in urban areas varied according to different scenarios. Specifically, 4.71 km² of urban land were inundated in the scenario predicting urban growth, 4.01 km² in the scenario with no change in urban area, and 3.96 km² in the scenario with urban shrinkage, all based on the LULC maps for 2030. With a 7.2 m rise in water levels, the 2030 urbanization-based LULC maps project that 49.91 km² (27%) of the total 185.17 km² of urban areas will be flooded. In contrast, the stagnant urban-based LULC map for 2030 shows 42.52 km² (32%) of the total 132.79 km² at risk, and the shrinkage-based LULC map for the same year indicates 42.31 km² (33.7%) of the total 125.32 km² will be affected by flooding.

The embankment functions as a vital flood defense for the coastal belt. Nevertheless, Kashima Port, Kamisu City, along with Nakaminato Port, portions of Kawamatacho City, and areas adjacent to the port in Oarai City were heavily affected by flooding, experiencing the greatest impact within the region.

4. Discussion

Analyzing Japan's future urban processes amidst an unprecedented demographic shift due to population contraction with environmental changes such as sea-level rise from climate change is crucial. This analysis includes exploring the scenario-based effects of shrinkage alongside infrastructure and redevelopment measures in urban areas in response to high coastal tide and wave levels, which is essential for developing more resilient urban oceanfronts. Such a comprehensive understanding is vital for fostering more resilient urban oceanfronts in the face of these challenges. Understanding the confluence of complex and dynamic future land-use changes with flood hazards is essential to developing a resilient city seaside. The current study highlights that computational, scenario-based assessment is a practical and integrative approach to handling these complexities, necessary for sustainable urban planning and disaster mitigation. By anticipating these changes, this method becomes instrumental in identifying the most vulnerable locations, forming the basis for planning and designing flood risk mitigation efforts. This ensures Japan's urban and rural landscapes' resilience, functionality, and adaptability to changing demographic and environmental conditions.

4.1. Assessment and Associated Limitations of the Proposed Methodology

The proposed method offers a thorough and practical solution for forecasting land use transformation maps, encompassing scenarios from urban expansion to stabilization and decline. This approach includes assessing flood impacts at two specific water levels, 4 m, and 7.2 m, as outlined in Ibaraki's coastal conservation plan, and applying these assessments to 2030 maps for defense and disaster mitigation purposes. To accurately represent and analyze the intricate aspects and nonlinear relationships affecting future urban characteristics and population changes, we developed indicators focusing on topography, accessibility, and population data. Notably, we incorporated some emerging and new factors like population change rates (considering past and future trends), the spatial distribution of the population aged 65 and over, and detailed patterns of initial pixel transition probabilities (prior to their historical changes) derived from a maximum entropy classifier. These factors help to broadly understand the patterns of development and decline in the coastal areas of Ibaraki Prefecture by 2030 from a generalized perspective. Our hybrid ANN-MC model effectively amalgamates all explanatory variables with land-use changes, resulting in more accurate simulation outcomes. Additionally, we produced a roughness map and embankments, culminating in flood simulations and subsequent analysis using LULC maps. This study highlights the importance of assessing future flood risks in the context of climate, land use, and population changes, offering key insights for spatial planning adjustments. The uncertainties of this approach are the limited spatial resolution inherent in population forecast data. Moreover, the development and integration

of spatial distribution data for vacant houses, along with similar data for key economic indicators such as average income and GDP per capita, can be instrumental in enriching the analysis. Nevertheless, the framework's outputs are generally within acceptable boundaries, demonstrating its usefulness for anticipating potential coastal flooding hazards in the future.

4.2. Review of LULC Modeling Outcomes

Our research indicates that the most pronounced land-use changes, characterized by the growth or shrinkage of urban areas, predominantly occurred in agricultural regions. Notably, new residential developments tended to emerge near existing homes or close to population centers, in contrast to the more dispersed pattern of declining residential areas. In towns like Nakaminato, Oarai, Okushicho, Itako, and Kamisu, residential zones showed no signs of shrinkage. Despite a halt in population growth, urban expansion continues, driven by factors such as housing market dynamics, an increase in per capita living space due to smaller family sizes, and the development of infrastructure, including the rise of solar farms. This expansion persists amidst population decline, resulting in denser urban areas and subsequent infrastructure development. The expansion approach has shown higher accuracy in forecasting urban expansion, reflecting a trend of ongoing growth in urban regions. The natural log transformation of proximity to residential areas and their morphological characteristics emerged as key predictive variables for future urban development. This implies that understanding the physical constraints was important for urban expansion, and lower-elevation areas were more developed. Furthermore, natural logarithm transformation, particularly for distance variables, is a standard method to normalize data, especially in skewed distributions.

Moreover, our findings suggest that the demographic distribution, mainly the population aged over 65, influences both the decline and stabilization of urban areas. The rate of population change is another significant factor in anticipating urban decline. This conveys that this dynamic variable can capture both growth and decline, providing a nuanced view of how population shifts influence land use in the model. Also, the output of the maximum entropy classifier was a key complementary input to the ANN model throughout scenarios. Considering that, in this research the altered pixels map was employed as the dependent variable in this regression model, thereby providing the probability distribution for every transition in the historical context based on the independent variables. So, it can precisely track subtle land cover changes. It proves that a retrospective approach that reveals how strongly each change agent was historically related to the transition probability of a pixel is quite helpful.

In the projected grassland expansion scenario, our findings suggest an ongoing trend where cropland and paddy fields are predominantly transformed into grasslands. Specifically, an area of 18.78 m² of cropland and 9.76 m² of paddy fields is expected to be converted into grassland.

4.3. Flood Simulation Results

To achieve "zero victims", it is essential to address various flood scales. The Ibaraki Coastal Protection Basic Plan cites the worst-case scenario as an H2 event with water heights ranging from 4 m to a maximum of 7.2 m. Flood simulations are based on these high tide levels. Our result indicates that embankments along Ibaraki's coastline, standing at a height of 4 m, successfully protected against flooding. However, a detailed examination of two major ports in the area showed mixed results. In Kashima, the embankments largely held back the floodwaters, but the port's entrance allowed water to seep through, leading to flooding in nearby residential zones. On the other hand, the areas densely populated around the Hinuma River in Nakaminato were entirely submerged. It was observed that densely populated residential areas, ranging from 4.71 to 4.01 and 3.96 km², were affected by flooding in each LULC scenario.

Earlier, we discussed that 7.2 m. peak level, anticipated in Hirai Kashima City and Hikawa Kamisu City, represents an extreme case scenario for many other coastal areas. Therefore, the results from these specific cities are crucial and hold more importance than those from other parts of the study area. The water level surged to 7.2 m, marginally surpassing the embankment height at various points along the coastline. As the water advanced towards Kashima port, the severity of the overtopping intensified, leading to flooding in numerous urban areas adjacent to the coast. Under LULC Scenarios 1 to 3, the area affected by residential flooding expanded significantly, recording increases of 45.2, 38.51, and 38.35 km², respectively, compared to previous levels. Such a huge disaster is poised to result in considerable economic damage and significant human losses, profoundly impacting the lives and livelihoods of people in the region.

Mao et al. [62] combined a hydraulic model with social media data to assess flood hazards in an urban area, focusing on the effects of urbanization and land subsidence on flood extent and depth. Their results revealed that changes in land use, elevation, and river water levels significantly altered flood extents over 1970–2019. So, emphasizing the need to predict coastal land use as a baseline map to evaluate the effects of flooding on this map for defense and conservation. Such data are indispensable for directing preemptive flood risk mitigation and shaping environmental management policies in the designated region.

The study by Tursina et al. [63] evaluates tsunami risks in Banda Aceh, incorporating land-use changes over 50 years and a projected sea-level rise. It uses the Markov chain and cellular automata for trend analysis and future predictions, respectively. Six land use types are identified and applied in tsunami simulations with the COMCOT model. Findings show a substantial impact on coastal urban areas, emphasizing the importance of coastal planning against future sea-level rise.

According to our current knowledge, there is no research that simulates the urban trajectory in Ibaraki's coastal area with population fluctuations while also predicting and assessing future floods caused by exacerbated high tides and waves on LULC 2030. These findings encourage interdisciplinary collaboration among stakeholders and authorities for effective flood risk management. Considering future urban and environmental developments, policies should focus on resilience and adaptability, offering enhanced cost benefits through a nonlinear, iterative review process.

4.4. Future Work

The forthcoming task entails conducting a simulation considering rainfall and upstream inflow and determining a roughness coefficient based on building characteristics, LULC change-induced permeability change, vegetation, and seasonal variations. Furthermore, there is a need for additional research in the future, particularly when more solid data on vacant properties and an improved resolution of future population distribution become available.

5. Conclusions

Coastal zones, subject to multifaceted influences, are susceptible to environmental changes from anthropogenic activities and natural phenomena that affect regional economies and ecological resilience, manifesting local repercussions. Climate-induced flood risks pose a threat to residents, underscoring the importance of forecasting coastal land use and assessing flood impacts for defense and conservation. Japan expects significant demographic decreases, and this demands a reassessment of their land-use change and its complex impacts. Therefore, evaluating Japan's urban trajectories is vital, as future strategies need to redefine urban transformation, considering the country's unique demographic trends.

The Ibaraki Coastal region is used as a case study to explore the probable implications of land-use changes and urban processes in 2030 and also predict and assess future floods caused by exacerbated high tides and waves. The scenario-based simulations show that the built-up area is increasing by 52.37 km² (39%) since 2020. Additionally, under a

hypothetical scenario where urban expansion remains constant, we observed an increase of 28.54 km² (42%) in grassland areas. In a contrasting scenario where urban areas contract, we noted a decrease of 7.47 km² (5.6%) in urban land cover over these ten years. Proximity to residential areas and their morphological characteristics are key predictors for future urban development, indicating a trend towards more condensed urban environments. Demographic distribution, especially regarding the population aged over 65, affects urban decline and stabilization. Population change rate is also a significant factor in anticipating urban decline. This trend indicates that the demographic shift has led to a negative spiral, making cities less attractive to younger populations, and further accelerating the decline. In a projected scenario, cropland and paddy fields are transforming into grasslands, with approximately 18.78 m² of cropland and 9.76 m² of paddy fields expected to be converted. This change highlights the growing trend of cropland abandonment, driven by a decreasing population.

Our findings also indicate that urban flooding varies depending on scenarios at a peak height of 4 m, which is the lower limit of the maximum run-up height due to storm surge expected in the study area. In the urban growth scenario, 4.71 sq. km of residential areas were flooded, while 4.01 sq. km were inundated in the stagnant scenario and 3.96 sq. km in the urban shrinkage scenario based on 2030 LULC maps. With the upper limit of 7.2 m, which is the extreme case in most of the study area, these areas increased to 49.91 sq. km, 42.52 sq. km, and 42.31 sq. km, respectively. Notable details of these outcomes imply the sensitivity of urban flooding to urbanization patterns and a significant increase in flooded areas for storm surge higher than the upper limit of the assumption.

From an adaptive urban planning viewpoint, employing a scenario-based flood risk assessment combined with a future land-use change model offers a multi-dimensional perspective on urban development trajectories and their associated challenges. This kind of analysis is crucial for guiding proactive flood risk reduction strategies and informing the development of environmental management policies within the targeted region.

Author Contributions: Conceptualization, M.S.; methodology, M.S.; software, M.S.; validation, M.S.; formal analysis, M.S.; investigation, M.S.; resources, M.S. and H.T.; data curation, M.S.; writing—original draft preparation, M.S.; writing—review and editing, H.T.; visualization, M.S.; supervision, H.T.; project administration, H.T.; funding acquisition, H.T. All authors have read and agreed to the published version of the manuscript.

Funding: This research was funded by the Environmental Research and Technology Development Fund of the Environmental Restoration and Conservation Agency of Japan (JPMEERF20S11811).

Institutional Review Board Statement: Not applicable.

Informed Consent Statement: Not applicable.

Data Availability Statement: Data is contained within the article.

Acknowledgments: We gratefully acknowledge the support from the Environmental Research and Technology Development Fund of the Environmental Restoration and Conservation Agency of Japan (JPMEERF20S11811).

Conflicts of Interest: The authors declare no conflicts of interest.

References

1. Wang, X.-J.; Tuo, Y.; Li, X.-F.; Feng, G.-L. Features of the new climate normal 1991–2020 and possible influences on climate monitoring and prediction in China. *Adv. Clim. Chang. Res.* **2023**, *14*, 930–940. [[CrossRef](#)]
2. Syvitski, J.P.M.; Vörösmarty, C.J.; Kettner, A.J.; Green, P. Impact of humans on the flux of terrestrial sediment to the global coastal ocean. *Science* **2005**, *308*, 376–380. [[CrossRef](#)]
3. Hinkel, J.; Lincke, D.; Vafeidis, A.T.; Perrette, M.; Nicholls, R.J.; Tol, R.S.J.; Marzeion, B.; Fettweis, X.; Ionescu, C.; Levermann, A. Coastal flood damage and adaptation costs under 21st century sea-level rise. *Proc. Natl. Acad. Sci. USA* **2014**, *111*, 3292–3297. [[CrossRef](#)] [[PubMed](#)]
4. Syvitski, J.P.M.; Kettner, A.J.; Overeem, I.; Hutton, E.W.H.; Hannon, M.T.; Brakenridge, G.R.; Day, J.; Vörösmarty, C.; Saito, Y.; Giosan, L.; et al. Sinking deltas due to human activities. *Nat. Geosci.* **2009**, *2*, 681–686. [[CrossRef](#)]

5. Tabari, H. Climate change impact on flood and extreme precipitation increases with water availability. *Sci. Rep.* **2020**, *10*, 13768. [[CrossRef](#)]
6. Meehl, G.A.; Hu, A.; Tebaldi, C.; Arblaster, J.M.; Washington, W.M.; Teng, H.; Sanderson, B.M.; Ault, T.; Strand, W.G.; White, J.B., III. Relative outcomes of climate change mitigation related to global temperature versus sea-level rise. *Nat. Clim. Chang.* **2012**, *2*, 576–580. [[CrossRef](#)]
7. de Graaf, R.; Hooimeijer, F. (Eds.) *Urban Water in Japan*; CRC Press: Boca Raton, FL, USA, 2008.
8. Zhai, G.; Ikeda, S. Empirical analysis of Japanese flood risk acceptability within multi-risk context. *Nat. Hazards Earth Syst. Sci.* **2008**, *8*, 1049–1066. [[CrossRef](#)]
9. Srinivasan, T.N.; Gopi Rethinaraj, T.S. Fukushima and thereafter: Reassessment of risks of nuclear power. *Energy Policy* **2013**, *52*, 726–736. [[CrossRef](#)]
10. Suppasri, A.; Shuto, N.; Imamura, F.; Koshimura, S.; Mas, E.; Yalciner, A.C. Lessons learned from the 2011 great east japan tsunami: Performance of tsunami countermeasures, coastal buildings, and tsunami evacuation in japan. *Pure Appl. Geophys.* **2013**, *170*, 993–1018. [[CrossRef](#)]
11. Carter, J.G.; Cavan, G.; Connelly, A.; Guy, S.; Handley, J.; Kazmierczak, A. Climate change and the city: Building capacity for urban adaptation. *Prog. Plan.* **2015**, *95*, 1–66. [[CrossRef](#)]
12. Wu, X.; Wang, Z.; Guo, S.; Liao, W.; Zeng, Z.; Chen, X. Scenario-based projections of future urban inundation within a coupled hydrodynamic model framework: A case study in Dongguan City, China. *J. Hydrol.* **2017**, *547*, 428–442. [[CrossRef](#)]
13. Reckien, D.; Salvia, M.; Heidrich, O.; Church, J.M.; Pietrapertosa, F.; De Gregorio-Hurtado, S.; D’Alonzo, V.; Foley, A.; Simoes, S.G.; Krkoška Lorencová, E.; et al. How are cities planning to respond to climate change? Assessment of local climate plans from 885 cities in the EU-28. *J. Clean. Prod.* **2018**, *191*, 207–219. [[CrossRef](#)]
14. Lai, C.; Shao, Q.; Chen, X.; Wang, Z.; Zhou, X.; Yang, B.; Zhang, L. Flood risk zoning using a rule mining based on ant colony algorithm. *J. Hydrol.* **2016**, *542*, 268–280. [[CrossRef](#)]
15. Zhao, L.; Liu, F. Land-use planning adaptation in response to SLR based on a vulnerability analysis. *Ocean Coast. Manag.* **2020**, *196*, 105297. [[CrossRef](#)]
16. Canters, F.; Vanderhaegen, S.; Khan, A.Z.; Engelen, G.; Uljee, I. Land-use simulation as a supporting tool for flood risk assessment and coastal safety planning: The case of the Belgian coast. *Ocean Coast. Manag.* **2014**, *101*, 102–113. [[CrossRef](#)]
17. Berry, M.; BenDor, T.K. Integrating sea level rise into development suitability analysis. *Comput. Environ. Urban Syst.* **2015**, *51*, 13–24. [[CrossRef](#)]
18. Miller, M.M.; Shirzaei, M. Assessment of future flood hazards for southeastern Texas: Synthesizing subsidence, sea-level rise, and storm surge scenarios. *Geophys. Res. Lett.* **2021**, *48*, e2021GL092544. [[CrossRef](#)]
19. Feng, Y.; Yang, Q.; Hong, Z.; Cui, L. Modelling coastal land use change by incorporating spatial autocorrelation into cellular automata models. *Geocarto Int.* **2018**, *33*, 470–488. [[CrossRef](#)]
20. Lai, C.; Chen, X.; Wang, Z.; Yu, H.; Bai, X. Flood risk assessment and regionalization from past and future perspectives at basin scale. *Risk Anal.* **2020**, *40*, 1399–1417. [[CrossRef](#)] [[PubMed](#)]
21. Moya, L.; Mas, E.; Koshimura, S. Learning from the 2018 western Japan heavy rains to detect floods during the 2019 Hagibis typhoon. *Remote Sens.* **2020**, *12*, 2244. [[CrossRef](#)]
22. Liu, W.; Fujii, K.; Maruyama, Y.; Yamazaki, F. Inundation assessment of the 2019 Typhoon Hagibis in Japan using multi-temporal Sentinel-1 intensity images. *Remote Sens.* **2021**, *13*, 639. [[CrossRef](#)]
23. Ohki, M.; Yamamoto, K.; Tadono, T.; Yoshimura, K. Automated processing for flood area detection using ALOS-2 and hydrodynamic simulation data. *Remote Sens.* **2020**, *12*, 2709. [[CrossRef](#)]
24. Hattori, K.; Kaido, K.; Matsuyuki, M. The development of urban shrinkage discourse and policy response in Japan. *Cities* **2017**, *69*, 124–132. [[CrossRef](#)]
25. Bloom, D.E.; Chatterji, S.; Kowal, P.; Lloyd-Sherlock, P.; McKee, M.; Rechel, B.; Rosenberg, L.; Smith, J.P. Macroeconomic implications of population ageing and selected policy responses. *Lancet* **2015**, *385*, 649–657. [[CrossRef](#)]
26. Hartt, M.D. How cities shrink: Complex pathways to population decline. *Cities* **2018**, *75*, 38–49. [[CrossRef](#)]
27. Ma, Z.; Zhou, G.; Zhang, J.; Liu, Y.; Zhang, P.; Li, C. Urban shrinkage in the regional multiscale context: Spatial divergence and interaction. *Sustain. Cities Soc.* **2024**, *100*, 105020. [[CrossRef](#)]
28. Peng, W.; Wu, Z.; Duan, J.; Gao, W.; Wang, R.; Fan, Z.; Liu, N. Identifying and quantizing the non-linear correlates of city shrinkage in Japan. *Cities* **2023**, *137*, 104292. [[CrossRef](#)]
29. Housing and Land Survey. Available online: <https://www.stat.go.jp/english/data/jyutaku/index.html> (accessed on 8 January 2024).
30. Infrastructure Supporting Life and Economy, ‘Growing’ Ibaraki. Available online: <https://www.pref.ibaraki.jp/soshiki/doboku/stock.html> (accessed on 8 January 2024).
31. Nguyen Hao, Q.; Takewaka, S. Shoreline changes along northern Ibaraki Coast after the Great East Japan Earthquake of 2011. *Remote Sens.* **2021**, *13*, 1399. [[CrossRef](#)]
32. Coastal Conservation Master Plan. Available online: <https://www.pref.ibaraki.jp/doboku/kasen/coast/032000.html> (accessed on 8 January 2024).
33. High-Resolution Land-Use and Land-Cover Map of Japan. Available online: https://www.eorc.jaxa.jp/ALOS/en/dataset/lulc/lulc_v2111_e.htm (accessed on 8 January 2024).

34. GSI Maps. Available online: <https://maps.gsi.go.jp/> (accessed on 8 January 2024).
35. WorldPop Hub. Available online: <https://hub.worldpop.org/> (accessed on 8 January 2024).
36. Future Estimated Population Data by 500 m Mesh (H29 National Political Bureau Estimates). Available online: <https://nlftp.mlit.go.jp/ksj/gml/datalist/KsjTmplt-mesh500.html> (accessed on 8 January 2024).
37. DioVISTA/Flood. Available online: <https://www.hitachi-power-solutions.com/en/service/digital/diovista-flood/index.html> (accessed on 8 January 2024).
38. Shafizadeh-Moghadam, H.; Tayyebi, A.; Ahmadlou, M.; Delavar, M.R.; Hasanlou, M. Integration of genetic algorithm and multiple kernel support vector regression for modeling urban growth. *Comput. Environ. Urban Syst.* **2017**, *65*, 28–40. [[CrossRef](#)]
39. Inouye, C.E.N.; de Sousa, W.C., Jr.; de Freitas, D.M.; Simões, E. Modelling the spatial dynamics of urban growth and land use changes in the north coast of São Paulo, Brazil. *Ocean Coast. Manag.* **2015**, *108*, 147–157. [[CrossRef](#)]
40. Peng, W.; Fan, Z.; Duan, J.; Gao, W.; Wang, R.; Liu, N.; Li, Y.; Hua, S. Assessment of interactions between influencing factors on city shrinkage based on geographical detector: A case study in Kitakyushu, Japan. *Cities* **2022**, *131*, 103958. [[CrossRef](#)]
41. Bernt, M. The limits of shrinkage: Conceptual pitfalls and alternatives in the discussion of urban population loss: Debates & developments. *Int. J. Urban Reg. Res.* **2016**, *40*, 441–450.
42. Döringer, S.; Uchiyama, Y.; Penker, M.; Kohsaka, R. A meta-analysis of shrinking cities in Europe and Japan. Towards an integrative research agenda. *Eur. Plan. Stud.* **2020**, *28*, 1693–1712. [[CrossRef](#)]
43. Hori, K.; Saito, O.; Hashimoto, S.; Matsui, T.; Akter, R.; Takeuchi, K. Projecting population distribution under depopulation conditions in Japan: Scenario analysis for future socio-ecological systems. *Sustain. Sci.* **2021**, *16*, 295–311. [[CrossRef](#)]
44. Kubo, T.; Yui, Y. *The Rise in Vacant Housing in Post-Growth Japan*; Springer: Singapore, 2019; 175p.
45. Zhang, Y.; Fu, Y.; Kong, X.; Zhang, F. Prefecture-level city shrinkage on the regional dimension in China: Spatiotemporal change and internal relations. *Sustain. Cities Soc.* **2019**, *47*, 101490. [[CrossRef](#)]
46. Sarkar, D.; Saha, S.; Mondal, P. GIS-based frequency ratio and Shannon's entropy techniques for flood vulnerability assessment in Patna district, Central Bihar, India. *Int. J. Environ. Sci. Technol.* **2022**, *19*, 8911–8932. [[CrossRef](#)]
47. Htet, H.; Khaing, S.S.; Myint, Y.Y. Tweets sentiment analysis for healthcare on big data processing and IoT architecture using maximum entropy classifier. In *Advances in Intelligent Systems and Computing*; Springer: Singapore, 2019; pp. 28–38.
48. Safabakhshpachehkenari, M.; Tonooka, H. Assessing and enhancing predictive efficacy of machine learning models in urban land dynamics: A comparative study using multi-resolution satellite data. *Remote Sens.* **2023**, *15*, 4495. [[CrossRef](#)]
49. Haghghat, F. Predicting the trend of indicators related to COVID-19 using the combined MLP-MC model. *Chaos Solitons Fractals* **2021**, *152*, 111399. [[CrossRef](#)]
50. Mansour, S.; Ghoneim, E.; El-Kersh, A.; Said, S.; Abdelnaby, S. Spatiotemporal monitoring of urban sprawl in a coastal city using GIS-based Markov Chain and artificial Neural Network (ANN). *Remote Sens.* **2023**, *15*, 601. [[CrossRef](#)]
51. Saeidi, S.; Mohammadzadeh, M.; Salmanmahiny, A.; Mirkarimi, S.H. Performance evaluation of multiple methods for landscape aesthetic suitability mapping: A comparative study between Multi-Criteria Evaluation, Logistic Regression and Multi-Layer Perceptron neural network. *Land Use Policy* **2017**, *67*, 1–12. [[CrossRef](#)]
52. Bratley, K.; Ghoneim, E. Modeling urban encroachment on the agricultural land of the Eastern Nile Delta using remote sensing and a GIS-based Markov Chain model. *Land* **2018**, *7*, 114. [[CrossRef](#)]
53. Lin, W.; Sun, Y.; Nijhuis, S.; Wang, Z. Scenario-based flood risk assessment for urbanizing deltas using future land-use simulation (FLUS): Guangzhou Metropolitan Area as a case study. *Sci. Total Environ.* **2020**, *739*, 139899. [[CrossRef](#)]
54. Smirnova, D.A.; Medvedev, I.P. Extreme Sea Level Variations in the Sea of Japan Caused by the Passage of Typhoons Maysak and Haishen in September 2020. *Russ. Acad. Sci. Oceanol.* **2023**, *63*, 623–636. [[CrossRef](#)]
55. Yamaguchi, S.; Ikeda, T.; Iwamura, K. Rapid flood simulation software for personal computer with Dynamic Domain Defining Method. In Proceedings of the 4th International Symposium on Flood Defence: Managing Flood Risk, Reliability and Vulnerability, Toronto, ON, Canada, 6–8 May 2008.
56. Connell, R.J.; Painter, D.J.; Beffa, C. Two-dimensional flood plain flow. II: Model validation. *J. Hydrol. Eng.* **2001**, *6*, 406–415. [[CrossRef](#)]
57. Yamaguchi, S.; Ikeda, T.; Yamaho, S. Flood risk assessment system for major metropolitan areas in Japan. In Proceedings of the 10th International Conference on Hydroinformatics (HIC 2012), Hamburg, Germany, 14–18 July 2012.
58. Yamaguchi, S.; Ikeda, T. Automatic integration of hydraulic and hydrologic models based on geographic information. In Proceedings of the 9th International Conference on Hydroinformatics (HIC 2010), Tianjin, China, 7–11 September 2010.
59. Xia, Y. Chapter Eleven—Correlation and association analyses in microbiome study integrating multiomics in health and disease. *Prog. Mol. Biol. Transl. Sci.* **2020**, *171*, 309–491.
60. Mogaraju, J.K. Artificial Intelligence assisted prediction of land surface temperature (LST) based on significant air pollutants over the Annamayya district of India. *Res. Sq.* **2023**. [[CrossRef](#)]
61. Available online: https://www.mlit.go.jp/river/shishin_guideline/kaigan/takashioshinsui_manual.pdf (accessed on 30 April 2023).

62. Ouyang, M.; Kotsuki, S.; Ito, Y.; Tokunaga, T. Employment of hydraulic model and social media data for flood hazard assessment in an urban city. *J. Hydrol. Reg. Stud.* **2022**, *44*, 101261. [[CrossRef](#)]
63. Tursina, S.; Kato, S.; Afifuddin, M. Incorporating dynamics of land use and land cover changes into tsunami numerical modelling for future tsunamis in Banda Aceh. *E3S Web Conf.* **2022**, *340*, 01014. [[CrossRef](#)]

Disclaimer/Publisher's Note: The statements, opinions and data contained in all publications are solely those of the individual author(s) and contributor(s) and not of MDPI and/or the editor(s). MDPI and/or the editor(s) disclaim responsibility for any injury to people or property resulting from any ideas, methods, instructions or products referred to in the content.